Light scattering by hexagonal ice crystals: comparison of finite-difference time domain and geometric optics models

Ping Yang and K. N. Liou

Department of Meteorology/Center for Atmospheric and Remote Sounding Studies, University of Utah, Salt Lake City, Utah 84112

Received June 7, 1994; revised manuscript received August 22, 1994; accepted August 23, 1994

We have developed a finite-difference time domain (FDTD) method and a novel geometric ray-tracing model for the calculation of light scattering by hexagonal ice crystals. In the FDTD method we use a staggered Cartesian grid with the implementation of an efficient absorbing boundary condition for the truncation of the computation domain. We introduce the Maxwell–Garnett rule to compute the mean values of the dielectric constant at grid points to reduce the inaccuracy produced by the staircasing approximation. The phase matrix elements and the scattering efficiencies for the scattering of visible light by two-dimensional long circular ice cylinders match closely those computed from the exact solution for size parameters as large as 60, with maximum differences less than 5%. In the new ray-tracing model we invoke the principle of geometric optics to evaluate the reflection and the refraction of localized waves, from which the electric and magnetic fields at the particle surface (near field) can be computed. Based on the equivalence theorem, the near field can subsequently be transformed to the far field, in which the phase interferences are fully accounted for. The phase functions and the scattering efficiencies for hexagonal ice crystals computed from the new geometric ray-tracing method compare reasonably well with the FDTD results for size parameters larger than approximately 20. When absorption is involved in geometric ray tracing, the adjusted real and imaginary refractive indices and Fresnel formulas are derived for practical applications based on the fundamental wave theory.

1. INTRODUCTION

Information about the single-scattering properties of nonspherical ice crystals is fundamental to an understanding of radiative transfer in high-level clouds and the radiation budget of the Earth-atmosphere system. Interpretation of the bidirection radiance data obtained from space observations also requires knowledge of the scattering characteristics of ice particles. From *in situ* aircraft observations it has been shown that a large portion of ice crystals occurring in the Earth's atmosphere has a hexagonal structure.[1] This is also evident from observations of halos associated with cirrus clouds. The importance of ice in the atmosphere with respect to remote sensing and climate modeling has been articulated by Liou,[2] Liou and Takano,[3] and Stephens *et al.*[4]

It appears unlikely that an exact solution for the scattering by hexagonal particles can be derived because an appropriate coordinate system for the boundary condition at the particle surface cannot be imposed. For this reason research on light scattering by hexagonal ice crystals in the past two decades has used the principles of geometric optics in terms of the ray-tracing technique to determine the scattering and polarization properties of hexagonal ice particles.[5–12] Geometric ray tracing has been employed to identify the optical phenomena occurring in the atmosphere.[10,11] More recently, scattering properties for more complex ice crystal shapes have also been determined by the geometric ray-tracing method.[13,14] In the limit of the geometric optics a light beam may be thought of as consisting of a bundle of separate rays that hits the particle. Each ray will then undergo reflection and refraction and will pursue its own path along a straight line. However, the laws of geometric optics may be applied to scattering of light if the particle with a locally smooth surface is much larger than the incident wavelength. It has been estimated that the geometric optics approximation should be valid for size parameters larger than approximately 30–40.[15] Although numerous methods, including the discrete-dipole approximation,[16,17] the extended boundary condition method,[18] and the integral equation technique,[19,20] have been developed for the solution of light scattering by nonspherical particles, they are usually applicable to size parameters smaller than approximately 10–15 in the three-dimensional case. It is evident that single-scattering properties for hexagonal ice crystals with size parameters less than approximately 30 do not exist. In particular, there is a void of scattering information for size parameters between approximately 10 and 30. In light of the preceding discussion, there is a practical necessity to develop a light-scattering methodology that can be applied effectively to this size parameter range and that one can use as a reference to determine the applicability of the conventional geometric ray-tracing approximation for the computation of light scattering by hexagonal ice crystals.

In this paper we present the finite-difference time domain (FDTD) approach for the solution of light scattering by hexagonal ice particles. In addition, a novel geometric optics model has also been developed for the calculation of scattering properties of hexagonal ice particles. In Section 2 the principle of FDTD is outlined, and an improved absorbing boundary condition associated with FDTD is described. The new geometric optics approximation based on the equivalent theorem is presented in Section 3, where we also discuss the absorption effect

0740-3232/95/010162-15$06.00

in geometric optics. Numerical results are reported in Section 4, in which the results computed from the FDTD method are compared with those from the exact solution for light scattering by circular cylinders. Relative accuracies of the phase function and the scattering efficiencies computed from the geometric optics approximations are presented with respect to the FDTD results for the size parameters of hexagonal ice particles from 10 to 40. Finally, conclusions are given in Section 5.

2. FINITE-DIFFERENCE TIME DOMAIN METHOD

Pioneered by Yee[21] in 1966, the FDTD method has been used extensively to solve various kinds of electromagnetic problems.[22–27] With the development of a number of highly absorbing boundary conditions in the late 1970's and 1980's,[28–32] the usefulness of the FDTD method in dealing with the scattering by an arbitrarily shaped or inhomogeneous object has been widely recognized. In recent years significant efforts have been focused on constructing the FDTD numerical schemes on curvilinear grids and nonorthogonal target-conforming grids.[27,33–37] Researchers have carried out these endeavors to avoid the staircasing approximation of an oblique surface in a rectangular mesh. The numerical schemes based on computational fluid dynamics[38,39] have also received considerable attention for some special electromagnetic problems, such as the propagation of a pulse in which a steep gradient appears. Although target-conforming schemes are more accurate, they are relatively inflexible when scatterers of various sizes and shapes are considered. In addition, the cells in a globally irregular mesh usually differ so greatly in size that one must use a small time increment in order to obtain stable solutions. Further, the irregular schemes are inherently more complicated and tedious. Ice, unlike metal, is not so different from vacuum in terms of electromagnetic properties. For this reason the staircasing does not pose a serious problem in our study, provided that a proper method is used in the evaluation of the dielectric constant over the grid. We find that the rectangular Cartesian grid is most appropriate for the present investigation. In what follows, we shall outline the procedure for the FDTD method and discuss improvements in conjunction with light scattering by long cylinders.

A. Time-Stepping Scheme for the Near Field

The scattering of light by an infinitely long cylinder with normal illumination is a two-dimensional (2-D) problem. It is an excellent approximation for the scattering of normal incident light by a cylinder whose length is much larger than its radius. In this case an arbitrarily polarized wave can be decomposed into TM- and TE-polarized waves. The source-free Maxwell equations can be written in component forms for the TM-polarized case as follows:

$$\frac{\epsilon(x,y)}{c}\frac{\partial E_z(x,y,t)}{\partial t}=\frac{\partial H_y(x,y,t)}{\partial x}-\frac{\partial H_x(x,y,t)}{\partial y}, \tag{1a}$$

$$\frac{1}{c}\frac{\partial H_x(x,y,t)}{\partial t}=-\frac{\partial E_z(x,y,t)}{\partial y}, \tag{1b}$$

$$\frac{1}{c}\frac{\partial H_y(x,y,t)}{\partial t}=\frac{\partial E_z(x,y,t)}{\partial x}, \tag{1c}$$

where ϵ is the permittivity and c is the speed of light. The permeability is taken as $\mu = 1$ because the scatterer in our study is nonferromagnetic. The axis of the cylinder has been chosen to be normal to the xy plane. Similarly, for the TE-polarized case we have

$$\frac{1}{c}\frac{\partial \tilde{H}_z(x,y,t)}{\partial t}=\frac{\partial E_y(x,y,t)}{\partial x}-\frac{\partial E_x(x,y,t)}{\partial y}, \tag{2a}$$

$$\frac{\epsilon(x,y)}{c}\frac{\partial E_x(x,y,t)}{\partial t}=-\frac{\partial \tilde{H}_z(x,y,t)}{\partial x}, \tag{2b}$$

$$\frac{\epsilon(x,y)}{c}\frac{\partial E_y(x,y,t)}{\partial t}=\frac{\partial \tilde{H}_z(x,y,t)}{\partial x}, \tag{2c}$$

where $\tilde{H}_z(x,y,t)$ is taken as $-H_z(x,y,t)$ so that the signs in Eqs. (1) and (2) are symmetrical.

Equations (1) and (2) are the governing equations for the total field. Because the electric properties of the medium in our consideration are linear, the total field is the superposition of incident field and induced field that is produced by the presence of the scattering object. If the incident wave is taken as a plane wave propagating along the x axis, then the equations for the incident wave in the TM case can be written in the form

$$\frac{1}{c}\frac{\partial E_z^o(x,t)}{\partial t}=\frac{\partial H_y^o(x,t)}{\partial x}, \tag{3a}$$

$$\frac{1}{c}\frac{\partial H_y^o(x,t)}{\partial t}=\frac{\partial E_z^o(x,t)}{\partial x}, \tag{3b}$$

where the superscript o denotes the incident wave.

Using Eqs. (1) and (3) and the linear superposition property of the field, one can express the equations governing the induced field (denoted by the superscript s) for the TM case by

$$\frac{\epsilon(x,y)}{c}\frac{\partial E_z^s(x,y,t)}{\partial t}=\frac{\partial H_y^s(x,y,t)}{\partial x}-\frac{\partial H_x^s(x,y,t)}{\partial y}-[\epsilon(x,y)-1]\frac{\partial H_y^o(x,t)}{\partial x}, \tag{4a}$$

$$\frac{1}{c}\frac{\partial H_x^s(x,y,t)}{\partial t}=-\frac{\partial E_z^s(x,y,t)}{\partial y}, \tag{4b}$$

$$\frac{1}{c}\frac{\partial H_y^s(x,y,t)}{\partial t}=\frac{\partial E_z^s(x,y,t)}{\partial y}. \tag{4c}$$

For application to numerical computations Eqs. (4) must be discretized. We define a number of small square cells with a size Δs for the spatial domain. Integrating the left- and right-hand sides of Eq. (4a) over the cell centered at $(x,y) = (i,j)\Delta s$ leads to

$$\iint_{\mathrm{cell}(i,j)}\frac{\epsilon(x,y)}{c}\frac{\partial E_z^s(x,y,t)}{\partial t}\,dx\,dy\approx\frac{\overline{\epsilon}_{ij}}{c}\frac{\partial E_z^s(i,j,t)}{\partial t}\Delta s^2, \tag{5a}$$

$$\iint_{\mathrm{cell}(i,j)} \left[\frac{H_y^s(x, y, t)}{\partial x} - \frac{H_x^s(x, y, t)}{\partial y} \right] \mathrm{d}x\mathrm{d}y$$

$$- \iint_{\mathrm{cell}(i,j)} \left[\frac{\partial H_y^o(x, t)}{\partial x} \right] [\epsilon(x, y) - 1] \mathrm{d}x\mathrm{d}y$$

$$\approx \Delta s[H_x^s(i, j - 1/2, t) - H_x^s(i, j + 1/2, t) + H_y^s(i + 1/2, j, t) - H_y^s(i - 1/2, j, t)] - \Delta s(\bar{\epsilon}_{ij} - 1)[H_y^o(i + 1/2, t) - H_y^o(i - 1/2, t)]. \quad (5b)$$

In relations (5) the permittivity $\bar{\epsilon}_{ij}$ is the mean value over the cell (i, j). In our computations we use the Maxwell–Garnett rule[19] to obtain this value through

$$\frac{\bar{\epsilon}_{ij} - 1}{\bar{\epsilon}_{ij} + 2} = \frac{1}{\Delta s^2} \iint_{\mathrm{cell}(i,j)} \frac{\epsilon(x, y) - 1}{\epsilon(x, y) + 2} \mathrm{d}x\mathrm{d}y. \quad (6)$$

Note that using the mean value of the permittivity in the computations over the grid cell will offset somehow the effect of the stepping approximation on the scatter.

Applying to Eq. (4) the above discretization procedures in space along with a leapfrog difference scheme for temporal variation, we obtain a set of finite-difference equations for the TM-polarized case as follows:

$$E_z^{s(n+1)}(i, j) = E_z^{s(n)}(i, j) + \frac{c\Delta t}{\Delta s \bar{\epsilon}_{ij}} \{[H_y^{s(n+1/2)}(i + 1/2, j) - H_y^{s(n+1/2)}(i - 1/2, j)] + [H_x^{s(n+1/2)}(1, j - 1/2) - H_x^{s(n+1/2)}(i, j + 1/2)]\} + \left(1 - \frac{1}{\bar{\epsilon}_{ij}}\right) \frac{c\Delta t}{\Delta s} \times [H_y^{o(n+1/2)}(i - 1/2) - H_y^{o(n+1/2)}(i + 1/2)], \quad (7a)$$

$$H_x^{s(n+1/2)}(i, j + 1/2) = H_x^{s(n-1/2)}(i, j + 1/2) + \frac{c\Delta t}{\Delta s} [E_z^{s(n)}(i, j) - E_z^{s(n)}(i, j + 1)], \quad (7b)$$

$$H_y^{s(n+1/2)}(i + 1/2, j) = H_y^{s(n-1/2)}(i + 1/2, j) + \frac{c\Delta t}{\Delta s} [E_z^{s(n)}(i + 1, j) - E_z^{s(n)}(i, j)], \quad (7c)$$

where the superscript n denotes the time step. The above equations represent the time-stepping variation of the pure scattered field for the TM-polarized wave. Similar expressions can be obtained for the TE case. Once the values of the field at the grid mesh are given, we can obtain those at the next time step by explicitly updating the finite-difference scheme. It should be pointed out that the results computed from the pure-scattered-field formulation do not differ significantly from those computed from the total-field formulation[23] because the present study does not involve heavily shielded cavities.

B. Boundary Condition for the Numerical Mesh

The actual scattering problem is one that is unbounded in space. However, in practice, the domain of numerical computations must be truncated, leading to the requirement of a boundary condition for the truncated domain. Mathematically, it is clear that the time iteration of the electric field at the boundary requires the values of the magnetic field that are outside the truncated domain if the spatial domain is cut off through the centers of certain cells. For this reason the electric field at the boundary cannot be provided by the iterative difference equations but must be given by an appropriate boundary condition so that the scattered wave would not be reflected back to the computational domain artificially. In conjunction with this, various kinds of absorbing boundary condition have been developed.[28–32] Among them, the second-order absorbing boundary condition developed by Mur[30] based on a one-way wave equation is often used for truncation of the numerical mesh. However, there are several disadvantages associated with this method. First, applying this second-order absorbing boundary condition involves the field at the mesh corners, where the truncation of the spatial domain does not permit implementation of the formulation. At the corners either a first-order absorbing boundary condition or an extrapolating scheme must be used. Second, the solution converges slowly with increasing white space if thesecond-order absorbing condition is used.[40] Last, the absorbing boundary conditions derived from the one-way wave equation are usually tedious, especially when higher orders are considered in the three-dimensional (3-D) case.

The transmitting boundary method, which was originally developed in studies of seismology and earthquake engineering, has been found to perform extremely well for transient-wave analyses.[28] When the values of the field in the boundary equation are not at nodal locations, a general expression of the boundary condition is given by the quadratic interpolation scheme; that is, for a boundary at x_1,

$$U(t + \Delta t, x_1) = \sum_{j=1}^{N} (-1)^{j+1} C_j^N \overline{T}^j \overline{U}_j, \quad (8)$$

where U is any component of the field evaluated by the boundary condition, C_j^N is a binomial coefficient, and $\overline{T}^j$ is given by

$$\overline{T}^j = \overline{T}^1 \begin{bmatrix} T_{j-1,1} & T_{j-1,2} & \cdots & \cdots & T_{j-1,2j-1} & 0 & 0 \\ 0 & T_{j-1,1} & T_{j-1,2} & \cdots & \cdots & T_{j-1,2j-1} & 0 \\ 0 & 0 & T_{j-1,1} & T_{j-1,2} & \cdots & \cdots & T_{j-1,2j-1} \end{bmatrix}, \quad j \geq 2, \quad (9)$$

$$\overline{T}^1 = [(2 - \beta)(1 - \beta)/2, \beta(2 - \beta), \beta(\beta - 1)/2], \quad (10)$$

where $\beta = c\alpha\Delta t/\Delta s$ and α is an artificial transmitting coefficient, defined as the ratio of the artificial transmitting speed to the real speed of the physical wave. The transpose of $\overline{U}_j$ on the right-hand side of Eq. (8) is defined by $\overline{U}_j^T = [U_{1,j}, U_{2,j}, \ldots, U_{2j+1,j}]$, where $U_{ij} = U(t_j, x_i)$, $x_i = x_1 - (i - 1)\Delta s$, and $t_j = t - (j - 1)\Delta t$. The above algorithm is the general form of the transmitting boundary condition developed by Liao *et al.*[28] We find that the second- or third-order formulations can yield accurate results in a number of FDTD calculations.

However, the algorithm is still rather tedious, in that the field at $2N + 1$ grid points is required for the Nth-order formulation. In what follows, we present a simpler formulation in conjunction with the FDTD method. The

basic version of the transmitting formula is given by[28]

$$U(t + \Delta t, x) = \sum_{j=1}^{N} (-1)^{(j+1)} C_j^N \times U[t - (j - 1)\Delta t, x - j\alpha c\Delta t]. \quad (11)$$

If the artificial transmitting coefficient α is chosen as unity and the time interval is properly selected so that the values of the field on the right-hand side of Eq. (11) are located at nodal points, the computation will become much more efficient. Moreover, if the cells in the numerical mesh are chosen to be squares (for the 2-D case) or cubes (for the 3-D case) with a size Δs, the Courant–Friedrichs–Levy conditions for the stability of the FDTD time-stepping algorithm are[22]

$$\frac{c\Delta t}{\Delta s} \le \frac{\sqrt{2}}{2} \approx 0.707, \qquad \text{2-D case}, \quad (12)$$

$$\frac{c\Delta t}{\Delta s} \le \frac{\sqrt{3}}{3} \approx 0.577, \qquad \text{3-D case}. \quad (13)$$

Thus, if we choose $c\Delta t = 0.5\Delta s$ for a generous stability condition, the values of the field in Eq. (11) may be selected to locate at nodal points, leading to a simplified formula for the transmitting boundary. For example, at the left-hand boundary the second-order transmitting boundary condition can be written as

$$U^{(n+1)}(1, j) = 2U^{(n-1)}(2, j) - U^{(n-3)}(3, j), \quad (14)$$

and the third-order condition can be expressed by

$$U^{(n+1)}(1, j) = 3U^{(n-1)}(2, j) - 3U^{(n-3)}(3, j) + U^{(n-5)}(4, j). \quad (15)$$

Although the third-order method is more accurate than the second-order method, it is slightly unstable in numerical computations. To stabilize the algorithm we may use the weighted superposition of Eqs. (14) and (15) in the form

$$U^{(n+1)}(1, j) = (3 - \gamma)U^{(n-1)}(2, j) - (3 - 2\gamma)U^{(n-3)}(3, j) + (1 - \gamma)U^{(n-5)}(4, j). \quad (16)$$

Using this weighted method and selecting a value of 0.1 for γ, we find that the algorithm is stable even for 10,000 steps of iteration. Since the boundary condition proposed here is simple and the boundary field at the previous time step is not required, the algorithm is very suitable for application of the super absorption technique,[41] designed to improve absorbing boundary conditions. In addition, it should be noted that there are no special requirements for the mesh corners if the transmitting boundary is used because the fields at the corners will not affect those at the interior grid points, as is evident from Eqs. (7).

C. Field in the Frequency Domain

The values of the near field computed by the above FDTD algorithm are in the time domain. In order to obtain the frequency response of the scatterer, we require a transform of the time-dependent fields to the corresponding fields in the frequency domain. For this purpose we use the Gaussian pulse propagating toward the scatterer as an incident wave, along with a Fourier transform. Because the size of the scatterer is fixed for a given execution in numerical computations, the Fourier transform at various frequencies (or wave numbers) will provide the scattered field in the frequency domain for different size parameters.

Let f be a component of the field and its value at the time step n be f_n. Then the time variation of f can be written as

$$f(t) = \sum_{n=0}^{N} f_n \delta(t - n\Delta t), \quad (17)$$

where δ is the Dirac delta function and the time step N is so chosen that the field in the domain of computation has been reduced significantly to a small value. The corresponding spectrum in the wave-number domain is given by

$$F(k) = \int_{-\infty}^{\infty} \left[\sum_{n=0}^{N} f_n \delta(t - n\Delta t) \right] \exp(ikct) \mathrm{d}t = \sum_{n=0}^{N} f_n \exp(ikcn\Delta t), \quad (18)$$

where k is the wave number in vacuum. To avoid aliasing and numerical dispersion and to obtain a correct frequency spectrum, one must band the maximum wave number or the minimum wavelength. Let the minimum wavelength permitted by the grid size Δs be $\lambda_{\min} = p2\pi\Delta s$. Because we have selected $c\Delta t/\Delta s = 1/2$, it follows that

$$F(k) = \sum_{n=0}^{N} f_n \exp(ink/2pk_{\max}), \quad (19)$$

where $k_{\max} = 2\pi/\lambda_{\min}$. Thus, for a desirable wave number $k = qk_{\max}$, where q is a real number between 0 and 1, the frequency spectrum is given by

$$F(k) = \sum_{n=0}^{N} f_n \exp(inq/2p). \quad (20)$$

If the radius of the scatterer is a, then the corresponding size parameter is $ka = aq/p\Delta s$. In numerical computations we may take a number of q and fix the other parameters so that the scattering fields for different size parameters can be obtained. Next, the input Gaussian pulse is represented in discrete form as

$$f_n = A \exp[-(n/w - 5)^2], \quad (21)$$

where A is a constant and w is a parameter controlling the width of the pulse. In the present study we have chosen w to be 30 to avoid the numerical dispersion that can occur in the pulse propagation. The center of the Gaussian distribution is shifted by $5w$ so that the pulse can start with a small value ($\sim 10^{-11}$) at the initial time.

D. Transformation of Near Field to Far Field

In order to obtain the scattering characteristic of the scatterer, we must transform the near-field properties

obtained from the FDTD method to those of the far field. Let us consider a curve that encloses the scatterer in a 2-D space. For the TM-polarized case the electric field at any location outside the curve can be expressed by[42]

$$E_z(\mathbf{r}) = \oint \hat{n} \cdot [E_z(\mathbf{r}')\nabla' G(\mathbf{r}, \mathbf{r}') - G(\mathbf{r}, \mathbf{r}')\nabla' E_z(\mathbf{r}')]\mathrm{d}r', \tag{22}$$

where the integral is along the enclosing curve, $\hat{n}$ is the outward unit vector normal to the curve, and G is Green's function for the 2-D case, which can be expressed in terms of the zero-order Hankel function of the first kind as follows:

$$G(\mathbf{r}, \mathbf{r}') = \frac{i}{4} H_0^{(1)}(|\mathbf{r} - \mathbf{r}'|), \qquad i = \sqrt{-1}. \tag{23}$$

For the far field we must have $k(|\mathbf{r} - \mathbf{r}'|) \to \infty$. Using the asymptotic behavior of the Hankel function, we have

$$E_z^s(\mathbf{r}) = \left(\frac{2}{\pi kr}\right)^{1/2} \exp[i(kr + 3\pi/4)]\frac{i}{4} \times \oint \left[ik(\hat{n} \cdot \hat{r})E_z^s(\mathbf{r}') + \frac{\partial E_z^s(\mathbf{r}')}{\partial n} \right] \times \exp(-ik\hat{r} \cdot \mathbf{r}')\mathrm{d}r', \tag{24}$$

where $\hat{r} = \mathbf{r}/|\mathbf{r}|$. In the numerical computation we find that one should discretize the derivative term in Eq. (24) by a fourth-order difference scheme in order to obtain high accuracy. For example, if $\hat{n}$ is along the x axis, this term is approximated by

$$\frac{\partial E_z^s}{\partial n}(i\Delta s, j\Delta s) = \frac{\partial E_z^s}{\partial x}(i\Delta s, j\Delta s) \approx \frac{4}{3}\frac{E_z^s(i+1, j) - E_z^s(i-1, j)}{2\Delta s} - \frac{1}{3}\frac{E_z^s(i+2, j) - E_z^s(i-2, j)}{4\Delta s}. \tag{25}$$

For a 2-D case with an arbitrarily polarized incident wave the scattering wave can be expressed in terms of the scattering matrix in the form

$$\begin{bmatrix} E_{\mathrm{TM}}^s \\ E_{\mathrm{TE}}^s \end{bmatrix} = \left(\frac{2}{\pi kr}\right)^{1/2} \exp[i(kr + 3\pi/4) - ikx] \times \begin{bmatrix} F_{\mathrm{TM}}(\hat{s}) & 0 \\ 0 & F_{\mathrm{TE}}(\hat{s}) \end{bmatrix} \begin{bmatrix} E_{\mathrm{TM}}^i \\ E_{\mathrm{TE}}^i \end{bmatrix}, \tag{26}$$

where $\hat{s}$ denotes the scattering direction and the matrix elements can be obtained from

$$F_{\mathrm{TM}}(\hat{s}) = \frac{i}{4}\frac{1}{|E_{\mathrm{TM}}^i|} \oint \left[\frac{\partial E_z^s(\mathbf{r}')}{\partial n} + ikE_z^s(\mathbf{r}')(\hat{n} \cdot \hat{s}) \right] \times \exp(-ik\hat{s} \cdot \mathbf{r}')\mathrm{d}r', \tag{27a}$$

$$F_{\mathrm{TE}}(\hat{s}) = \frac{i}{4}\frac{1}{|\tilde{H}_{\mathrm{TE}}^i|} \oint \left[\frac{\partial \tilde{H}_z^s(\mathbf{r}')}{\partial n} + ik\tilde{H}_z^s(\mathbf{r}')(\hat{n} \cdot \hat{s}) \right] \times \exp(-ik\hat{s} \cdot \mathbf{r}')\mathrm{d}r'. \tag{27b}$$

The nonzero elements of the corresponding Stokes matrix can then be expressed by[43]

$$P_{11}(\hat{s}) = \tfrac{1}{2}[|F_{\mathrm{TM}}(\hat{s})|^2 + |F_{\mathrm{TE}}(\hat{s})|^2], \tag{28a}$$

$$P_{12}(\hat{s}) = \tfrac{1}{2}[|F_{\mathrm{TM}}(\hat{s})|^2 - |F_{\mathrm{TE}}(\hat{s})|^2], \tag{28b}$$

$$P_{33}(\hat{s}) = \mathrm{Re}\{F_{\mathrm{TM}}(\hat{s}) \cdot [F_{\mathrm{TE}}(\hat{s})]^*\}, \tag{28c}$$

$$P_{34}(\hat{s}) = \mathrm{Im}\{F_{\mathrm{TM}}(\hat{s}) \cdot [F_{\mathrm{TE}}(\hat{s})]^*\}, \tag{28d}$$

where the asterisk denotes the complex conjugate.

For nonabsorbing cases the scattering (or extinction) cross section is given by the optical theorem as follows:

$$\sigma_{\mathrm{TM}} = \frac{4}{k}\,\mathrm{Re}[F_{\mathrm{TM}}(\hat{s})]_{\hat{s}=\hat{x}}, \tag{29a}$$

$$\sigma_{\mathrm{TE}} = \frac{4}{k}\,\mathrm{Re}[F_{\mathrm{TE}}(\hat{s})]_{\hat{s}=\hat{x}}, \tag{29b}$$

where $\hat{x}$ is the unit vector along the incidence direction.

3. NOVEL GEOMETRIC OPTICS MODEL

The principles of geometric optics may be applied to the scattering of light by a scatterer whose size is much larger than the incident wavelength. In this case light rays can be localized, and one can carry out geometric ray tracing to obtain the scattered energy. In the context of geometric optics, the total field is assumed to consist of the diffracted rays and the reflected and refracted rays, as shown in Fig. 1. The diffracted rays pass around the scatterer. The rays impinging on the scatterer undergo local reflection and refraction, referred to as Fresnelian interaction. The energy that is carried by the diffracted and the Fresnelian rays is assumed to be the same as the energy that is intercepted by the particle cross section projected along the incident direction. The intensity of the far-field scattered light within the small-scattering-angle interval $\Delta\Theta$ in the scattering direction Θ can be computed from the summation of the intensity contributed by each individual ray emerging in the direction between $\Theta - \Delta\Theta/2$ and $\Theta + \Delta\Theta/2$. Except in the method presented by Cai and Liou,[8] essentially all the conventional geometric ray-tracing techniques ignored phase interferences between relevant rays. It is usually assumed that the interference may be smoothed out when the particles are randomly oriented.[9] In this case the extinction efficiency of the scatterer is 2.

On the basis of Babinet's principle, diffraction by a scatterer may be regarded as that by an opening on an opaque

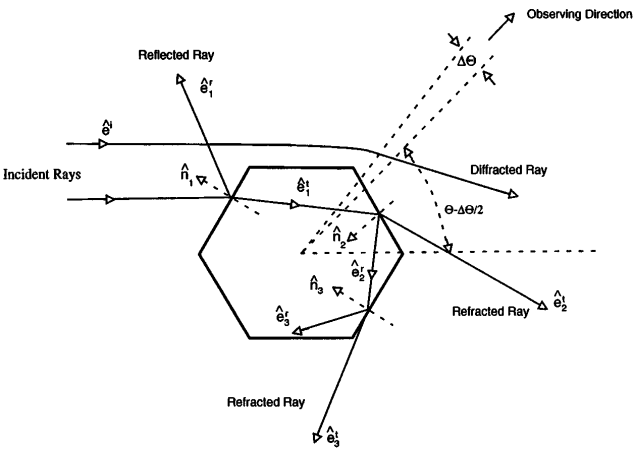

Fig. 1. Geometry for the conventional ray-tracing technique.

screen perpendicular to the incident light, which has the same geometric shape as the projected cross section of the scatterer. In the case of randomly oriented 2-D hexagonal ice crystals we can determine the diffraction intensity by using Fraunhofer diffraction with the normalized scattering phase function given by

$$P^d(\Theta) = \frac{1}{2\pi\chi}(1 + \cos\Theta)^2 \times \int_0^{\pi/6}\left[\frac{\chi\cos\alpha\sin(\chi\cos\alpha\sin\Theta)}{\chi\cos\alpha\sin\Theta}\right]^2 d\alpha, \quad (30)$$

where Θ is the scattering angle and $\chi = 2\pi a/\lambda$.

The reflection and refraction components are determined by the ray-tracing procedure. The directions of the rays denoted by the unit vectors shown in Fig. 1 can be determined by the equations

$$\hat{e}_p^r = \hat{e}_p^i - 2(\hat{e}_p^i \cdot \hat{n}_p)\hat{n}_p, \qquad p = 1, 2, 3, \ldots, \quad (31a)$$

$$\hat{e}_p^t = \frac{1}{m_p}\{\hat{e}_p^i - (\hat{e}_p^i \cdot \hat{n}_p)\hat{n}_p - [m_p^2 - 1 + (\hat{e}_p^i \cdot \hat{n}_p)^2]^{1/2}\hat{n}_p\}, \qquad p = 1, 2, 3, \ldots, \quad (31b)$$

$$\hat{e}_p^i = \begin{cases} \hat{e}^i, & p = 1 \\ \hat{e}_1^t, & p = 2 \\ \hat{e}_{p-1}^r, & p > 2 \end{cases}, \quad (31c)$$

where $m_p = m$ (refractive index of the scatterer) for $p = 1$ and $m_p = 1/m$ for $p > 1$. When ${m_p}^2 < 1 - (\hat{e}_p^i \cdot \hat{n}_p)^2$, total reflection occurs, and there will be no refracted ray. The electric field associated with the rays can be computed by the Fresnel formulas. Summing the energies of the rays that emerge within a small-scattering-angle interval in a given direction, we can obtain the phase function for this part. Let the normalized phase function that is due to reflection and refraction be $P^r(\Theta)$. Then the normalized phase function $P(\Theta) = [P^d(\Theta) + (2\tilde{\omega} - 1)P^r(\Theta)]/2\tilde{\omega}$, where $\tilde{\omega}$ is the single-scattering albedo.

The above discussion outlines the conventional geometric ray-tracing method. In numerical computation the polarization properties of the light rays must be considered. Following the procedures presented by Cai and Liou,[8] one can define and numerically compute the complete phase matrix associated with the four Stokes parameters and the scattering and absorbing cross sections.

The conventional ray-tracing technique requires the localization of the geometric rays. In addition, it also assumes the following: First, the scattering field is artificially decomposed into contributions from diffraction and Fresnelian rays, each of which contains 50% of the incident energy. Second, the vector property of the electromagnetic field is not completely accounted for because the Fraunhofer diffraction formulation in the context of geometric ray tracing is in scalar form. Moreover, the Kirchhoff assumption or Kirchhoff's boundary condition is required in the diffraction theory.[44] As discussed by Stratton and Chu,[45] the Kirchhoff assumption is not mathematically well posed as either a Dirichlet problem or a Neumann problem. As a result, the effect of the charges along the edge contour of the opening defined in the conventional method cannot be taken into consideration in the computation. Finally, calculations of the far field directly by ray tracing will produce a discontinuous distribution of the scattered energy, such as the delta transmission associated with 0° refraction produced by two parallel prismatic faces, as noted by Takano and Liou.[10]

A. Theory of Geometric Optics Model for Light-Scattering Calculations

To overcome the disadvantages in the geometric optics approach discussed above, we have developed a method to obtain the equivalent tangential electric and magnetic currents on the surface of the scatterer. One can then invoke these equivalent currents to solve the far field by means of the rigorous electromagnetic theory. As we show in Fig. 2, the wave front of the incident light beam is divided into a number of small wavelets or localized waves. We postulate that each of these wavelets propagates rectilinearly outside and inside the scatterer with the propagation deviation determined by Snell's law only at the surface. Therefore these wavelets behave as a plane wave locally. Subject to this postulation, the electric and magnetic fields associated with a certain wavelet would satisfy the transverse wave condition locally and can be expressed by

$$\mathbf{H} = m\hat{e} \times \mathbf{E} \qquad \text{inside the scatterer,} \quad (32a)$$

$$\mathbf{H} = \hat{e} \times \mathbf{E} \qquad \text{outside the scatterer,} \quad (32b)$$

where $\hat{e}$ is the unit vector along the propagating direction of the wavelet and can be determined by Eqs. (31a) and (31b). We can obtain the electric field by using the Fresnel formula and taking into account the phase differences. To illustrate the procedure for calculating the electric field at the surface, let us consider a vertically polarized incident wave for the 2-D case. Referring to Fig. 2, the incident wave at point Q_1 is given by

$$\mathbf{E}_i(\mathbf{r}_1) = A\hat{e}_z \exp(ik\hat{e}^i \cdot \mathbf{r}_1), \quad (33)$$

where A is the amplitude of the incident wave and $\hat{e}_z$ is a unit vector along the z axis (not shown in the diagram). The externally reflected electric field at the surface associated with the wavelet is given by

$$\mathbf{E}^r(\mathbf{r}_1) = R_1 A\hat{e}_z \exp(ik\hat{e}^i \cdot \mathbf{r}_1), \quad (34)$$

where R_1 is the Fresnel reflection coefficient. After the wavelet reaches point Q_2, a phase delay occurs, and the refracted electric field just outside the scatterer can be expressed by

$$\mathbf{E}^t(\mathbf{r}_2) = T_1 T_2 A\hat{e}_z \exp\{ik[\hat{e}^i \cdot \mathbf{r}_1 + m\hat{e}_1^t \cdot (\mathbf{r}_2 - \mathbf{r}_1)]\}, \quad (35)$$

where T_1 and T_2 are the Fresnel refraction coefficients at Q_1 and Q_2, respectively. The related magnetic fields can be obtained from Eqs. (32a) and (32b). Following this procedure, we can solve the sequential reflections and refractions for all the wavelets to obtain the total surface electric and magnetic fields. For example, the total surface electric field is given by

$$\mathbf{E}_{\text{total}}(\mathbf{r}) = \begin{cases} \mathbf{E}^i(\mathbf{r}) + \mathbf{E}^r(\mathbf{r}) + \mathbf{E}^t(\mathbf{r}), & \mathbf{r} \in \text{(illuminated surface)}, \\ \mathbf{E}^t(\mathbf{r}), & \mathbf{r} \in \text{(shadowed surface)}. \end{cases} \quad (36)$$

Since the total field may be regarded as a linear superposition of the incident field and the induced (or scattered) field that is due to the presence of a scatterer, it is clear from Eq. (36) that the scattered field on the shadowed surface is $\mathbf{E}^t(\mathbf{r}) - \mathbf{E}^i(\mathbf{r})$. The scattered waves on the shadowed surface of the particle will produce a strong forward-scattering peak that is due to phase interferences. We note that the surface field obtained from the above procedure is the same as that from the Kirchhoff approximation, which was first presented by Jackson[46] and applied to a scattering problem by Muinonen.[12] However, Muinonen simplified the Kirchhoff approximation in which the scalar Fraunhofer diffraction formula was used, and the phase interference was not accounted for in the numerical computation.

In applying the procedure to obtain the surface field, one must take into account appropriately the area illuminated by the incident and internally reflected wavelets. Let the width of the incident wavelet be σ^i. Then, for the external reflection, the area on the surface where the wavelet makes a contribution is

$$\sigma^r = -\sigma^i/(\hat{n}_1 \cdot \hat{e}^i). \tag{37}$$

For refraction after internal reflections of $p - 1$ the area can be proved to be

$$\sigma_p^t = \sigma^i[m^2 - 1 + (\hat{n}_1 \cdot \hat{e}^i)^2]^{1/2}[m(\hat{n}_1 \cdot \hat{e}^i)(\hat{n}_{p+1} \cdot \hat{e}_{p+1}^i)]^{-1}, \quad P \geq 1. \tag{38}$$

In Eqs. (37) and (38) all the unit vectors have the same definitions as they did in Eqs. (31).

After the surface fields are obtained, the equivalent surface tangential electric current $\mathbf{J}$ and the equivalent tangential magnetic current $\mathbf{M}$ can be defined as[23]

$$\mathbf{J}(\mathbf{r}) = \hat{n} \times \mathbf{H}(\mathbf{r}), \tag{39a}$$

$$\mathbf{M}(\mathbf{r}) = -\hat{n} \times \mathbf{E}(\mathbf{r}). \tag{39b}$$

Using the equivalent currents, one can obtain the far field. In the 2-D case the elements of the scattering matrix denoted in Eq. (26) can be expressed by

$$\begin{aligned} F_{\mathrm{TM}}(\hat{s}) &= \frac{k}{4}\oint[J_z(\mathbf{r}') - s_x M_y(\mathbf{r}') + s_y M_x(\mathbf{r}')] \\ &\quad \times \exp(-ik\hat{s} \cdot \mathbf{r}')\mathrm{d}r' \\ &= \frac{k}{4}\oint[n_x H_y(\mathbf{r}') - n_y H_x(\mathbf{r}') \\ &\quad - (\hat{n} \cdot \hat{s})E_z(\mathbf{r}')]\exp(-ik\hat{s} \cdot \mathbf{r}')\mathrm{d}r', \end{aligned} \tag{40a}$$

$$\begin{aligned} F_{\mathrm{TE}}(\hat{s}) &= \frac{k}{4}\oint[-M_z(\mathbf{r}') - s_x J_y(\mathbf{r}') + s_y J_x(\mathbf{r}')] \\ &\quad \times \exp(-ik\hat{s} \cdot \mathbf{r}')\mathrm{d}r' \\ &= \frac{k}{4}\oint[n_x E_y(\mathbf{r}') - n_y E_x(\mathbf{r}') \\ &\quad + (\hat{n} \cdot \hat{s})H_z(\mathbf{r}')]\exp(-ik\hat{s} \cdot \mathbf{r}')\mathrm{d}r', \end{aligned} \tag{40b}$$

where the amplitude of the incident wave is set as unity, n_x and n_y are the components of the surface normal vector, and the integration is performed along the contour of the scatterer surface. It should be pointed out that the new method is completely different from the conventional ray-tracing technique in the aspect of determining various cross sections. For extinction, scattering, and absorbing cross sections, only two of them are independent, and the third can be obtained from the other two on the basis of energy conservation. In the conventional ray-tracing technique the extinction efficiency is assumed to be 2, and the absorbing cross section is obtained by summation of the absorption of individual rays inside the particle. However, in the new method the extinction cross section is given by Eqs. (29), and the scattering cross section is determined by the fundamental expressions

$$\sigma_{\mathrm{TM}}^s = \frac{2}{\pi k}\int_0^{2\pi} |F_{\mathrm{TM}}(\Theta)|^2 \mathrm{d}\Theta, \tag{41a}$$

$$\sigma_{\mathrm{TE}}^s = \frac{2}{\pi k}\int_0^{2\pi} |F_{\mathrm{TE}}(\Theta)|^2 \mathrm{d}\Theta. \tag{41b}$$

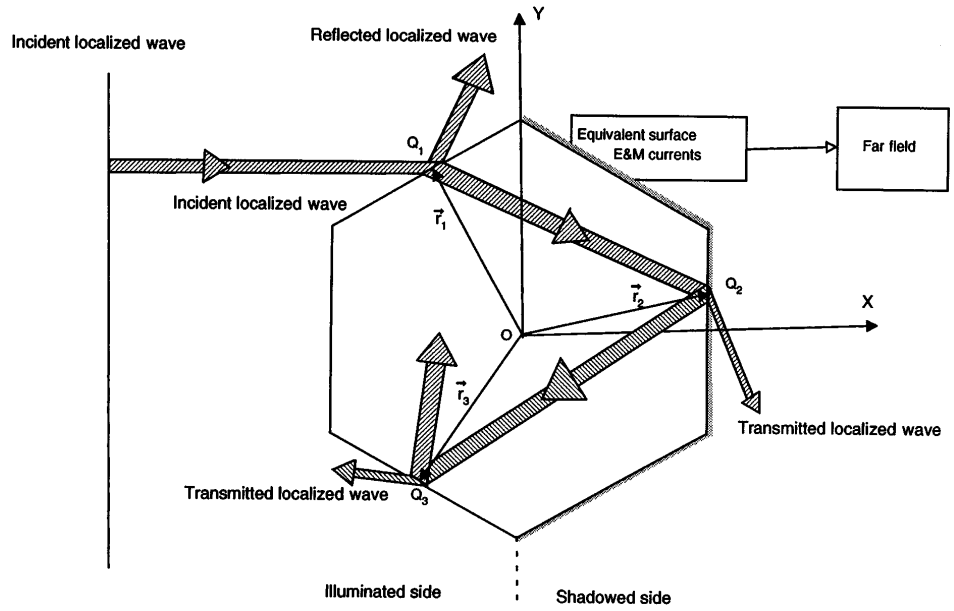

Fig. 2. Geometry for the new geometric optics model: E&M, electric and magnetic.

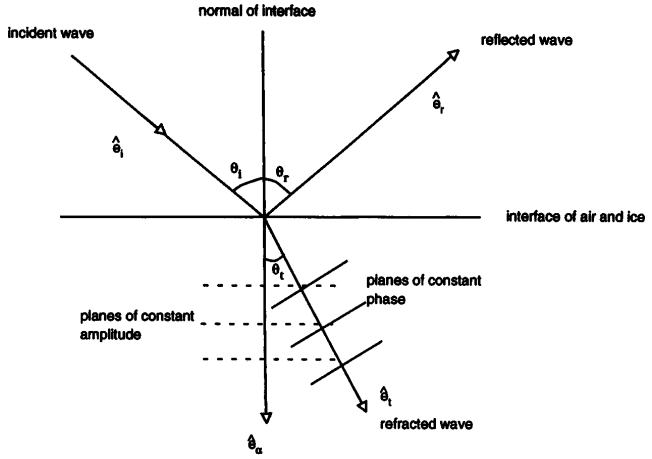

Fig. 3. Geometry for the inhomogeneity effect of the refracted wave in the absorptive case.

In light of the above discussion, the approximation in the improved geometric optics model comes from the calculation of the surface field by means of the geometric ray tracing. However, the transformation of the surface wave to the far field is exact. By the nature of the method the improved geometric optics model may be regarded as a hybrid method.

B. Absorption Effect in Geometric Optics

The geometric optics approach that has been used in the past generally assumes that the effect of absorption in the particle on the propagating direction of a ray can be neglected, so that the refracted angle and the ray path length can be computed from Snell's law and the geometry of the particle. This is a correct approach if the absorptions are small, such as those of ice and water in most of the solar wavelengths. For large-absorption cases rays refracted in the particle are almost totally absorbed. The geometric optics method can also be used in the computation of diffraction and external reflection as long as the particle size is much larger than the incident wavelength. Although the above argument is physically correct for small- and large-absorption cases, we shall consider the absorption effect in the context of geometric optics based on the fundamental electromagnetic wave theory and assess its relative importance in the ray-tracing calculation. Note that the effect of the complex refractive index on light beams has been formulated only in the Fresnel coefficients (see Born and Wolf[44]).

Consider the propagation of the incident wave from air to ice, as shown in Fig. 3. The wave vectors associated with the incident and reflected waves are real because these waves, which are outside the ice medium, must have the same properties. However, the wave vector of the refracted wave is complex; this is referred to as the inhomogeneity effect. These wave vectors can be represented by

$$\mathbf{k}_i = k_0\hat{e}_i, \qquad \mathbf{k}_r = k_0\hat{e}_r, \qquad \mathbf{k}_t = k_t\hat{e}_t + ik_\alpha\hat{e}_\alpha\,, \quad (42)$$

where $\hat{e}_i$, $\hat{e}_r$, $\hat{e}_t$, and $\hat{e}_\alpha$ are unit vectors defined in Fig. 3; the subscripts i, r, and t denote the incident, reflected, and refracted waves, respectively; $k_0 = 2\pi/\lambda$, where λ is the wavelength in air; and k_t and k_α are two real parameters that determine the complex wave vector of the refracted wave. For nonabsorptive cases k_α is zero. The corresponding electric vectors can be expressed by

$$\mathbf{E}_i(\mathbf{r}, t) = \mathbf{A}_i \exp[i(k_0\mathbf{r}\cdot\hat{e}_i - \omega t)], \quad (43a)$$

$$\mathbf{E}_r(\mathbf{r}, t) = \mathbf{A}_r \exp[i(k_0\mathbf{r}\cdot\hat{e}_r - \omega t)], \quad (43b)$$

$$\mathbf{E}_t(\mathbf{r}, t) = \mathbf{A}_t \exp\{i[(k_t\hat{e}_t + ik_\alpha\hat{e}_\alpha)\cdot\mathbf{r} - \omega t]\}, \quad (43c)$$

where $\mathbf{A}_i$, $\mathbf{A}_r$, and $\mathbf{A}_t$ are the amplitudes of these electric vectors, ω is the angular frequency, and $\mathbf{r}$ is a position vector. Further, we define the following parameters:

$$N_r = k_t/k_0, \qquad N_i^* = k_\alpha/k_0\,. \quad (44)$$

At the interface of the two media, at which the position vector is denoted as $\mathbf{r}_s$, the phases of the wave vibration must be the same for the incident, reflected, and refracted waves. Thus, from Eqs. (43) and (44), we obtain

$$\hat{e}_i\cdot\mathbf{r}_s = \hat{e}_r\cdot\mathbf{r}_s = N_r(\hat{e}_t\cdot\mathbf{r}_s) + iN_i^*(\hat{e}_\alpha\cdot\mathbf{r}_s)\,. \quad (45)$$

Since the wave vectors for the incident and reflected waves are real, we must have

$$\hat{e}_i\cdot\mathbf{r}_s = \hat{e}_r\cdot\mathbf{r}_s = N_r(\hat{e}_t\cdot\mathbf{r}_s)\,, \quad (46a)$$

$$\hat{e}_\alpha\cdot\mathbf{r}_s = 0\,. \quad (46b)$$

Based on the geometry illustrated in Fig. 3, Eq. (46a) represents a generalized form for the Snell law such that

$$\sin\Theta_i = \sin\Theta_r\,, \qquad \sin\Theta_t = \sin\Theta_i/N_r\,, \quad (47)$$

where Θ_i, Θ_r, and Θ_t denote the incident, reflected, and refracted angles, respectively, and Eq. (46b) implies that the vector $\hat{e}_\alpha$ is normal to the interface of the two media. Therefore it is clear from Eq. (43c) that the planes of constant amplitude of the refractive wave are parallel to the interface.

To determine N_r, we use the electric field of the refracted wave, which must satisfy the wave equation in the form

$$\nabla^2\mathbf{E}_t(\mathbf{r}, t) - \frac{(m_r + im_i)^2}{c^2}\frac{\partial^2\mathbf{E}_t(\mathbf{r}, t)}{\partial t^2} = 0\,, \quad (48)$$

where c is the speed of light in vacuum. Substituting Eq. (43c) into Eq. (48) and using Eqs. (44), we obtain

$$N_r^2 - N_i^{*2} = m_r^2 - m_i^2, \qquad N_rN_i^*\cos\Theta_t = m_rm_i\,. \quad (49)$$

Let $N_i = N_i^*\cos\Theta_t$; then we obtain from Eqs. (46) and (49) the following expressions:

$$N_r = \left\{\frac{m_r^2 - m_i^2 + \sin^2\Theta_i + [(m_r^2 - m_i^2 - \sin^2\Theta_i)^2 + 4m_r^2m_i^2]^{1/2}}{2}\right\}^{1/2}, \quad (50a)$$

$$N_i = m_rm_i/N_r\,. \quad (50b)$$

These two parameters are referred to as the adjusted real and imaginary refractive indices. After determining

N_r and N_i, one can write the refractive wave given in Eq. (43c) in the form

$$\mathbf{E}_t(\mathbf{r}, t) = \mathbf{A}_t \exp(-k_0 N_i l)\exp[i(k_0 N_r \hat{e}_t \cdot \mathbf{r} - \omega t)], \quad (51)$$

where $l = (\hat{e}_\alpha \cdot \mathbf{r})/\cos\Theta_t$ is the distance for the propagation of the refractive wave along the direction $\hat{e}_t$. It is clear that the direction of the phase propagation for the inhomogeneous wave inside the medium can be determined by N_r through Snell's law, and the attenuation of the wave amplitude during the wave propagation is determined by N_i. Consequently, the refracted wave can be traced precisely. In what follows, we shall derive the approximate Fresnel formula in conjunction with the inhomogeneous refracted wave. By letting $\mathbf{E}_t(\mathbf{r}) = \mathbf{A}_t \exp(-k_0 N_i l)$, we can rewrite Eq. (51) in the form

$$\mathbf{E}_t(\mathbf{r}, t) = \mathbf{E}_t(\mathbf{r})\exp[i(N_r k_0 \hat{e}_t \cdot \mathbf{r} - \omega t)]. \quad (52)$$

The corresponding magnetic vector is given by

$$\mathbf{H}_t(\mathbf{r}, t) = \mathbf{H}_t(\mathbf{r})\exp[i(N_r k_0 \hat{e}_t \cdot \mathbf{r} - \omega t)]. \quad (53)$$

Substituting Eqs. (52) and (53) into the Maxwell equations, we obtain

$$N_r \hat{e}_t \times \mathbf{H}_t(\mathbf{r}) + \epsilon \mathbf{E}_t(\mathbf{r}) = \frac{i}{k_0} \nabla \times \mathbf{H}_t(\mathbf{r}), \quad (54a)$$

$$N_r \hat{e}_t \times \mathbf{E}_t(\mathbf{r}) - \epsilon \mathbf{H}_t(\mathbf{r}) = \frac{i}{k_0} \nabla \times \mathbf{E}_t(\mathbf{r}), \quad (54b)$$

$$N_r \hat{e}_t \cdot \mathbf{E}_t(\mathbf{r}) = \frac{i}{k_0} \nabla \cdot \mathbf{E}_t(\mathbf{r}), \quad (54c)$$

$$N_r \hat{e}_t \cdot \mathbf{H}_t(\mathbf{r}) = \frac{i}{k_0} \nabla \cdot \mathbf{H}_t(\mathbf{r}), \quad (54d)$$

where the permeability has been taken as unity and $\sqrt{\epsilon} = m_r + i m_i$. From Eqs. (54c) and (54d) it is noted that the refracted wave is no longer a transverse wave with respect to the direction $\hat{e}_t$. The method of geometric optics is applicable to high-frequency waves.[44] In this case k_0 is very large, so that the terms on the right-hand sides of Eqs. (54) are much smaller than those on the left-hand sides. As a result, these imaginary terms may be neglected. However, in order to ensure that Eq. (54a) is a well-posed equation after the term on the right-hand side is neglected, we may take $\epsilon \approx N_r^2$, where $\sqrt{\epsilon} = m_r + i m_i$. Thus we have

$$\hat{e}_t \times \mathbf{H}_t(\mathbf{r}) + N_r \mathbf{E}_t(\mathbf{r}) \approx 0, \quad (55a)$$

$$N_r \hat{e}_t \times \mathbf{E}_t(\mathbf{r}) - \mathbf{H}_t(\mathbf{r}) \approx 0, \quad (55b)$$

$$\hat{e}_t \cdot \mathbf{E}_t(\mathbf{r}) \approx 0, \quad (55c)$$

$$\hat{e}_t \cdot \mathbf{H}_t(\mathbf{r}) \approx 0, \quad (55d)$$

where relations (55c) and (55d) are the transverse wave conditions that permit tracing of the electromagnetic fields associated with the rays. With the use of relations (55) the Fresnel reflection and refraction coefficients can be derived and are given by

$$R_l = \frac{N_r \cos\theta_i - \cos\theta_t}{N_r \cos\theta + \cos\theta_t}, \qquad T_l = \frac{2\cos\theta_i}{N_r \cos\theta_i + \cos\theta_t}, \quad (56a)$$

$$R_r = \frac{\cos\theta_i - N_r \cos\theta_t}{\cos\theta_i + N_r \cos\theta_t}, \qquad T_r = \frac{2\cos\theta_i}{\cos\theta_i + N_r \cos\theta_t}, \quad (56b)$$

where the subscripts l and r denote the horizontally and vertically polarized cases, respectively. Thus the inhomogeneity effect of the refracted wave may be accounted for approximately by adjustment of the refractive index. The simplification from Eqs. (54) to relations (55) implies that the inhomogeneous refracted wave can be approximated by a localized homogeneous plane wave whose wave front $\varphi(\mathbf{r})$ is determined by $\nabla^2\varphi(\mathbf{r}) = N_r^2$, which is the well-known eikonal equation in geometric optics,[44] and that the energy propagation of the localized wave is along the direction of $\hat{\phi} = \nabla\varphi/|\nabla\varphi| = \hat{e}_t$.

4. NUMERICAL RESULTS AND DISCUSSION

Light scattering by infinite circular cylinders with normal illumination can be solved analytically in terms of a series of cylindrical wave functions and computed by numerical means (referred to as the exact method). In order to verify the feasibility and the accuracy of the FDTD method, we have carried out numerical computations for the scattering of light by circular cylinders, using the FDTD and the exact methods. Comparisons are made for the phase matrix elements and the scattering efficiencies for the two polarization configurations.

Figure 4 shows the normalized phase function and three phase matrix elements for a size parameter of 20 and a refractive index of 1.31. For this size parameter the differences for the phase matrix elements computed from the two methods are within 0.3%. The total scattered energy computed by the FDTD method is approximately 0.9% less than that computed by the exact solution. The error in the FDTD method is caused mainly by a small amount of residual energy that, at the termination of the time-stepping iteration for the near field, remains inside the spatial domain enclosed by the curve on which the integration for the far field is defined. As we discussed in Section 2 above, the convergence of the near-field computation requires that the field inside the closed domain approach zero. However, a sufficiently long time period is required for exact convergence of the solution.

Figure 5 is the same as Fig. 4, except that the size parameter used is increased to 60. Again, the results computed by the FDTD method agree closely with those from the exact solution. Minor deviations occur in a number of side-scattering and backscattering directions at which the scattered energy is small. The errors for the phase matrix elements computed by the FDTD method are of the order of 1% with respect to the exact solution, except for the several directions mentioned above. In terms of the total scattered energy or the scattering efficiency, the FDTD results are approximately 3% less than the exact result. It is clear that the results for the size parameter 20 are better than those for the size parameter

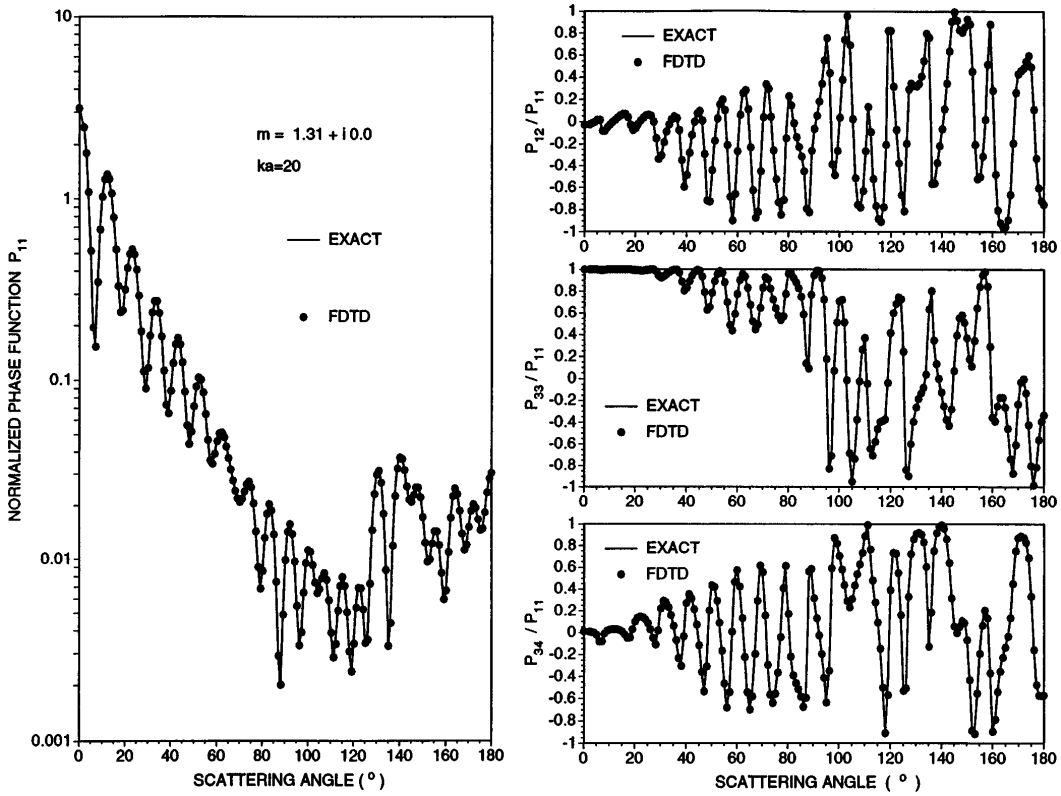

Fig. 4. Nonzero elements of the phase matrix for light scattering by a circular cylinder with a size parameter of 20.

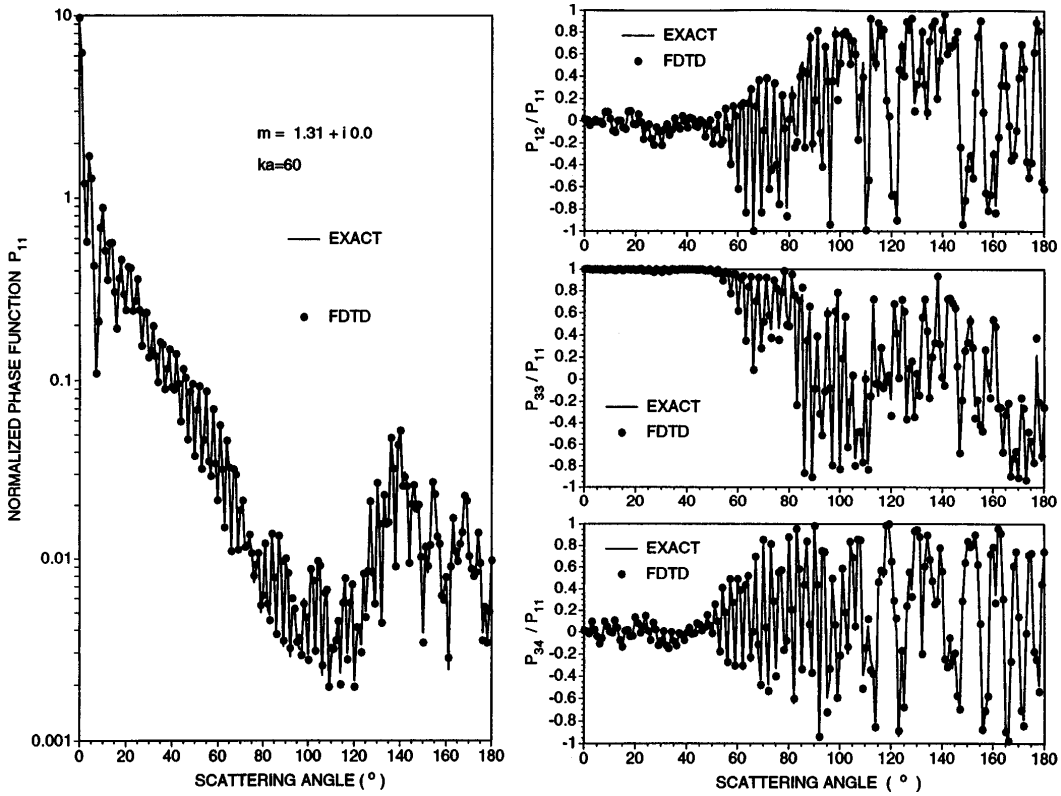

Fig. 5. Same as Fig. 4, except for a size parameter of 60.

60 because of the convergence requirement of the near-field computation.

In Fig. 6 are shown the scattering efficiencies as functions of the size parameter. A maximum error of approximately 5% is found for the size parameter 54. The fluctuating magnitude of the absolute error decreases as the size parameter decreases. The pattern of the error distribution may be understood from the fact

that the wavelength of the wave mode given by the Fourier transform of the pulse is inversely proportional to the size parameter, since the size of the particle is fixed in the computation. Also, the numerical dispersion and the error produced by the staircasing effect are smaller for longer wavelengths. Based on the results presented in Figs. 4–6, we conclude that FDTD is an accurate method for solving the scattering problem. In what follows, we use the FDTD results as references to investigate the accuracy of the geometric optics models.

In order to provide some quantitative knowledge of the accuracy and the applicable region of size parameters for the geometric ray-tracing technique, we have carried out the computations for the scattering of randomly oriented 2-D ice columns by using FDTD and geometric optics models. Figure 7 displays the normalized phase function computed by the convectional geometric ray-tracing method (GOM1), the new method (GOM2), and the FDTD method for the size parameters 20 and 40. Significant discrepancies are shown for the results computed by the GOM1 and the FDTD methods. For both size parameters the characteristics of the scattering patterns computed by the conventional ray-tracing technique do not agree with those produced by the FDTD method. In particular, the GOM1 method does not produce fluctuation patterns noted in the FDTD results that are associated with the phase configuration of the scattered wave. The assumption in the GOM1 method that one may smooth out the phase interference by averaging the particle orientations is not valid for the present cases. In comparison with the FDTD results, the relative error in the forward scattering computed by the GOM1 approach is approximately 98% for the size parameter 20 and 33% for the size parameter 40. It is clear that the Fraunhofer diffraction theory used in the GOM1 method is not a good approximation for size parameters smaller than 40.

For the size parameter 20 the results for the GOM2 method have similar fluctuating ripple structures to those for the FDTD method in the scattering region 0°–50°, although slightly larger values are produced by the GOM2 method. This implies that the phase configuration of the scattered wave determined by the GOM2 method is approximately correct in this region. It should be pointed out, however, that errors in the calculation of the wave amplitude cannot be avoided in the GOM2 approach because the Fresnel reflection and refraction coefficients are determined from the unbounded wave and interface. The relative difference for the forward scattering by the FDTD and GOM2 methods is approximately 10%. In terms of the total scattering energy, the relative error in the GOM2 method as compared with that of the FDTD method is also approximately 10%. When the size parameter increases to 40, the accuracy in the GOM2 method is much improved. The scattering patterns computed by the GOM2 method are very close to those computed by the FDTD method in the scattering region 0°–80°. The relative errors in the forward-scattering and the total scattering efficiency determined by the GOM2 method in this case are approximately 3% compared with those of the FDTD method. Thus, if the phase effect and the vector properties of the electromagnetic wave are accounted for, geometric optics can be accurately applied to the scattering by particles with size parameters larger than approximately 40. The GOM2 method is less accurate in the region around the backscattering direction. Although the cause of this is not entirely clear at this point, it is noted that the higher-order terms in the multipole expansion of the scattered field make significant contributions to the field in the

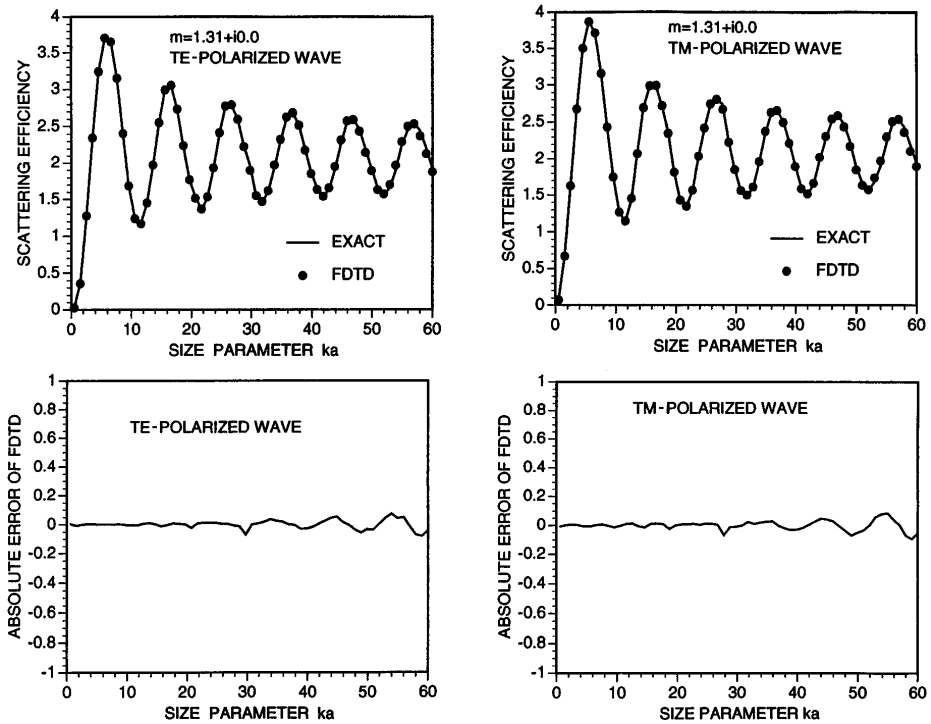

Fig. 6. Scattering efficiencies for the circular cylinders computed by the FDTD and the exact methods. Also shown are differences between the two.

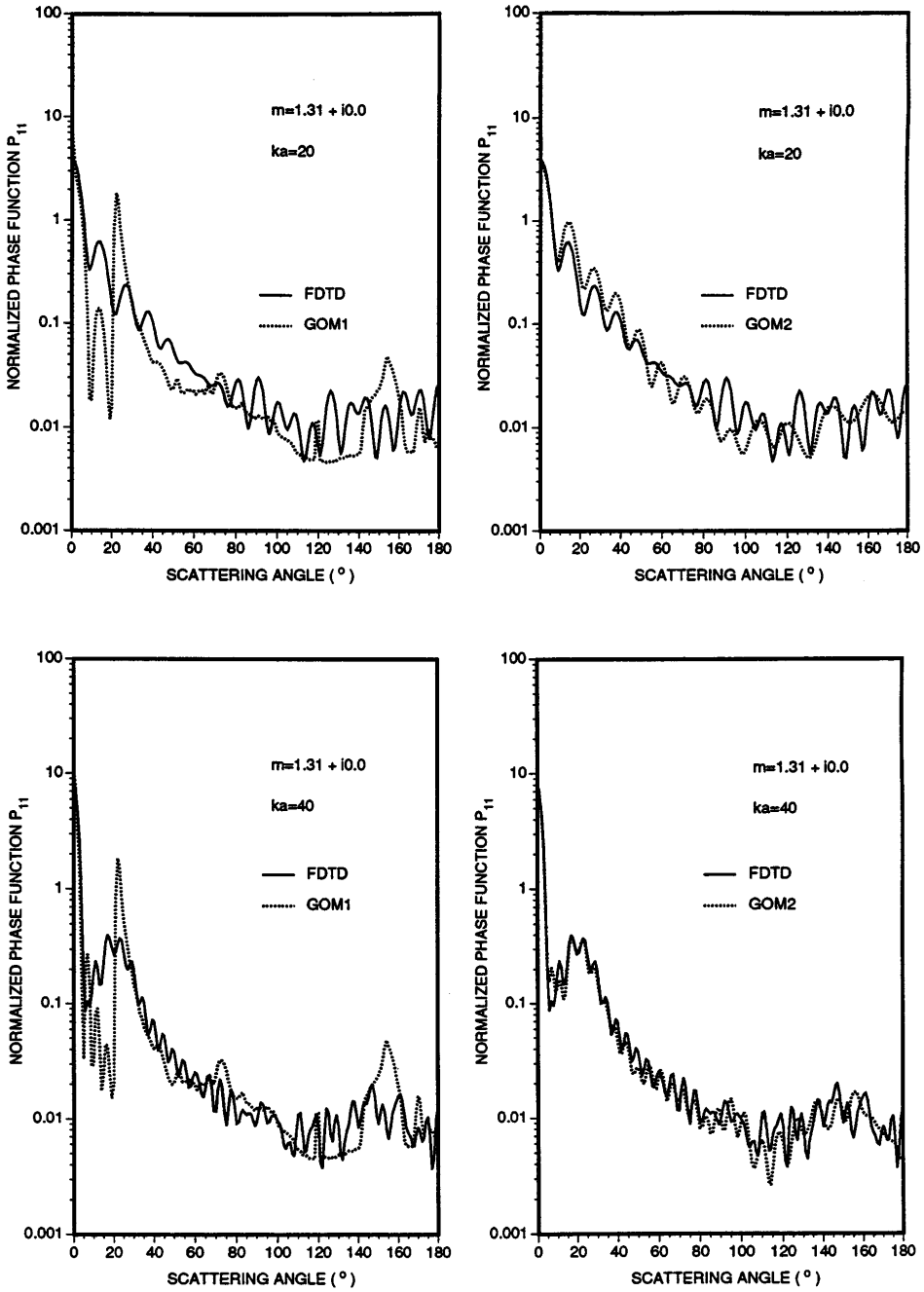

Fig. 7. Normalized phase functions computed by the FDTD, GOM1, and GOM2 methods for light scattering by randomly oriented 2-D hexagonal ice crystals.

backscattering direction that cannot be accounted for in geometric optics.[47]

In Fig. 8 we present that scattering efficiencies of randomly oriented 2-D hexagonal ice crystals for size parameters 10–40, using the FDTD, GOM1, and GOM2 methods. Deviations of the geometric optics results from FDTD solutions are also shown. The results obtained by the GOM1 method show large deviations because the conventional geometric optics is the asymptotic form of the rigorous electromagnetic theory for large size parameters. The assumption that the scattered energy in the nonabsorbing case contains two times the energy intercepted by the geometric cross section of the particle is not entirely correct for moderate size parameters. The new geometric optics method (GOM2) developed in this paper improves the accuracy of scattering efficiencies. The oscillating patterns in the scattering efficiency computed by the GOM2 method closely follow those computed by the FDTD method. The GOM2 results have relative errors of the order of 3% for the size parameter regions 23–28 and 35–40 and 10% for the size parameter regions 18–22 and 29–34. The maxima and minima errors approximately correspond to the scattering minima and maxima, respectively. We also note that the scattering maxima and minima computed by the GOM2 method slightly shift toward smaller size parameters with respect to the FDTD solution, but this shifting decreases with increasing size parameter. Significant GOM2 errors occur when size

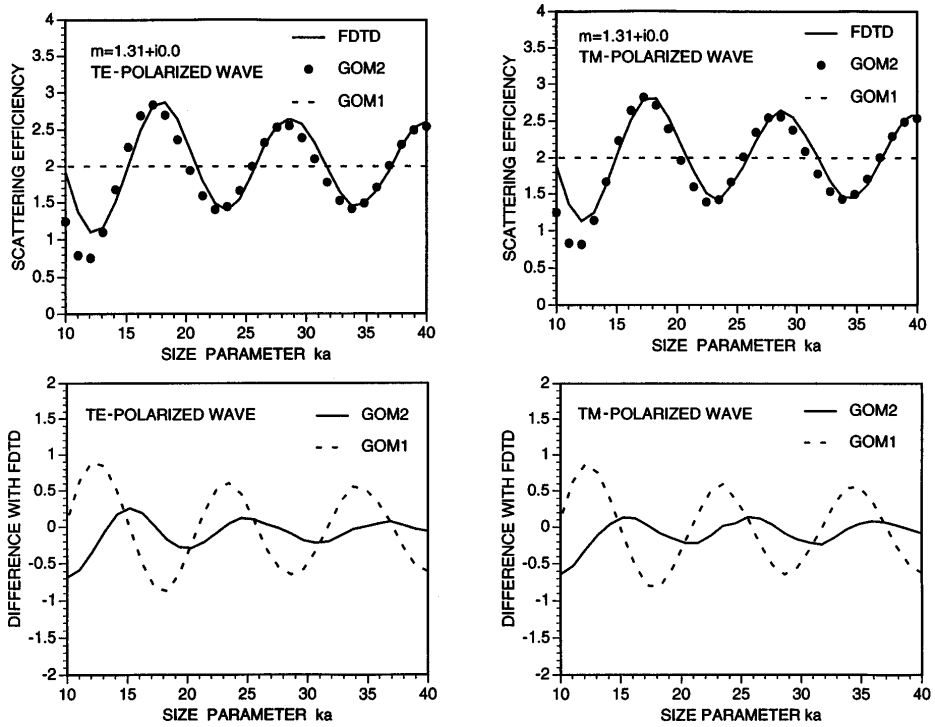

Fig. 8. Scattering efficiencies for randomly oriented 2-D hexagonal ice crystals and differences between GOM2 (GOM1) and FDTD results.

Table 1. Effect of Inhomogeneity of Refraction on the Single-Scattering Parameters for Size Parameters 40 and 100[a]

			Ka = 40						Ka = 100					
λ (μm)	m_r	m_i	Q_e	Q_e^*	$\tilde{\omega}$	$\tilde{\omega}^*$	g	g^*	Q_e	Q_e^*	$\tilde{\omega}$	$\tilde{\omega}^*$	g	g^*
0.1757	1.4511	1.0×10^{-5}	1.6001	1.6001	0.97457	0.97457	0.77887	0.77887	2.2968	2.2968	0.98933	0.98933	0.84330	0.84330
2.22	1.2604	2.21×10^{-4}	1.4433	1.4433	0.96949	0.96950	0.87711	0.87711	2.0567	2.0567	0.96862	0.96862	0.92079	0.92079
3.077	1.3251	6.25×10^{-1}	2.0000	2.0000	0.51384	0.51616	0.96377	0.96108	2.0000	2.0000	0.51828	0.52072	0.96708	0.96440
3.345	1.5413	6.68×10^{-2}	1.9955	1.9955	0.52739	0.52742	0.93031	0.93029	2.0000	2.0000	0.53306	0.53308	0.93406	0.93404
3.775	1.3873	6.6×10^{-3}	2.1574	2.1574	0.71380	0.71381	0.92525	0.92526	1.9755	1.9755	0.57082	0.57082	0.94598	0.94598
10.75	1.0908	1.68×10^{-1}	1.9787	1.9898	0.49747	0.49990	0.99054	0.98963	1.9915	1.9955	0.50231	0.50411	0.99376	0.99301
15.15	1.5667	1.64×10^{-1}	2.0000	2.0000	0.53017	0.53028	0.92657	0.92643	2.0000	2.0000	0.53483	0.53483	0.92998	0.92984

[a]The computations are carried out with GOM2. Asterisks denote that the adjusted refractive indices are used in the computations.

parameters are smaller than approximately 15, mainly because of the computation of the surface field by means of the geometric optics technique. In the GOM2 method we postulate that only the portion of the incident wave front that is in the region of the projected area of the particle interacts with the particle. This leads to a sharp division of the illuminated and shadowed sides of the particle surface. In a real situation variation of the field intensity on the particle surface from the illuminated side to the shadowed side is continuous because of the contribution of the part of the incident wave front outside the projected area of the particle. The effect of this phenomenon is significant for small particles and cannot be correctly handled by the GOM2 method. Nevertheless, the GOM2 method may be applied to size parameters larger than approximately 15 with acceptable accuracy. The improved accuracy of the GOM2 method in the computation of the scattering efficiency is significant for many practical applications, particularly for ice clouds that contain small ice crystals. Limited to the computer resources available at the time when the present investigation was conducted, we were able to carry out the FDTD computation for size parameters less than 40.

In Subsection 3.B we discussed the inhomogeneity of the refracted wave inside an absorbing particle. To illustrate this effect on the scattered field, we carried out computations of the single-scattering parameters, including extinction efficiency Q_e, single-scattering albedo $\tilde{\omega}$, and asymmetry factor g, for the size parameters 40 and 100 for a number of wavelengths for which ice has weak-

to-strong absorption, as shown in Table 1. For the cases involving weak absorption at the wavelengths 0.1757, 2.22, and 3.775 μm there is no detectable effect of the inhomogeneity on the scattered field. For the wavelengths 3.077, 3.345, 10.75, and 15.15 μm, in which large absorption occurs, the inhomogeneity effect on the single-scattering parameters is also negligible for both size parameters 40 and 100. Deviations occur only in the third to fourth digits. Although the inhomogeneity effect on the scattered field is insignificant for both cases, the mechanisms involved are quite different. For weak absorption the imaginary part of the refractive index is extremely small, so that the inhomogeneity effect on the refraction can be ignored. The inherent inhomogeneity of the refracted wave may be significant for the moderate- and strong-absorption cases. However, the wave that is refracted into the particle is essentially absorbed in these cases, and the absorption increases with the increase in the particle size. As a result, the scattered field is contributed mainly from the externally reflected wave. On the basis of the above discussion and the results presented in Table 1, we conclude that the absorption effect of ice on the calculation of the direction of refraction and the path length of the refracted wave can be neglected for wavelengths from 0.2 to 20 μm.

5. CONCLUSIONS

In this paper we have developed a finite-difference time domain (FDTD) technique and a novel geometric optics method for the calculation of light scattering by hexagonal ice crystals. We have also examined the effect of absorption on the refracted wave in the context of geometric ray tracing. The accuracy of the FDTD technique is first verified by a canonical problem involving the scattering of light by infinite circular cylinders for which an exact solution is available. For size parameters 0–60 it is shown that the errors produced by the FDTD technique are less than 5% in terms of the total scattered energy. The errors caused by the reflection of the artificial border and by the staircasing representation of the particle shape on a rectangular Cartesian grid appear to be negligible. As a reliable method, FDTD can be used as a reference for investigating the accuracy of the ray-tracing technique.

With respect to the geometric optics method, the conventional ray-tracing technique requires the light rays to be localized. Compared with the FDTD method, the conventional ray-tracing approach can produce significant errors for the scattering of light by ice crystals with size parameters smaller than 40, especially in the scattering angle regions near 22° and 154°, where the scattering peaks predicted by ray optics do not appear in the FDTD results. To circumvent the inherent problems in the conventional ray-tracing technique for light-scattering calculations, we have developed a novel hybrid method based on the equivalent theorem to compute the far field. For both phase functions and scattering efficiencies the new geometric optics approach produces accurate results for size parameters as small as 20. It is concluded that the phase configuration of the localized waves and the vector properties of the electromagnetic wave, which are not accounted for in the Fraunhofer diffraction theory, are important in determining the scattering by small ice crystals. Further, we have also investigated the inhomogeneity associated with the refracted waves inside an absorptive particle. The inhomogeneity effect on the scattered field has been shown to be insignificant for the cases of both weak and strong absorption.

The FDTD algorithm for light-scattering calculations for relatively large size parameters is very expensive in terms of both CPU time and memory requirement. It is unlikely to be a practical method for many applications at this point. For the scattering by randomly oriented 2-D hexagonal ice crystals with a size parameter of 40, we find that a CPU time of approximately 10 days is required by the FDTD method for a convergent solution on the Apollo Domain Series 10000 computer. On the other hand, the CPU time is less than 1 min for the GOM1 method and is approximately 0.5 h for the GOM2 method. Since the GOM2 method is applicable for size parameters larger than approximately 20, it will be a useful algorithm for calculating the single-scattering properties of naturally occurring ice crystals for most wavelengths in the solar and thermal infrared wavelengths. Investigations of the scattering of light by randomly oriented hexagonal ice crystals (3-D case) with the use of the FDTD and GOM2 methods are currently ongoing, and the results will be reported in a future paper.

ACKNOWLEDGMENTS

This study was supported by the Atmospheric Sciences Division of the National Science Foundation under grant ATM-93-15251.

Address correspondence to K. N. Liou (telephone: 801-581-3336; FAX: 801-581-4065).

REFERENCES

1. A. J. Heymsfield and R. G. Knollenberg, "Properties of cirrus generating cells," J. Atmos. Sci. **29,** 1358–1366 (1972).
2. K. N. Liou, "Influence of cirrus clouds on weather and climate process: a global perspective," Mon. Weather Rev. **114,** 1167–1199 (1986).
3. K. N. Liou and Y. Takano, "Light scattering by nonspherical particles: remote sensing and climatic implications," Atmos. Res. **31,** 271–298 (1994).
4. G. L. Stephens, S. C. Tsay, P. W. Stackhouse, and P. J. Flatau, "The relevance of the microphysical and radiative properties of cirrus clouds to climate and climate feedback," J. Atmos. Sci. **47,** 1742–1753 (1990).
5. H. Jacobowitz, "A method for computing transfer of solar radiation through clouds of hexagonal ice crystals," J. Quant. Spectrosc. Radiat. Transfer **11,** 691–695 (1971).
6. P. Wendling, R. Wendling, and H. K. Weickmann, "Scattering of solar radiation by hexagonal ice crystals," Appl. Opt. **18,** 2663–2671 (1979).
7. R. F. Coleman and K. N. Liou, "Light scattering by hexagonal ice crystals," J. Atmos. Sci. **38,** 1260–1271 (1981).
8. Q. Cai and K. N. Liou, "Polarized light scattering by hexagonal ice crystals: theory," Appl. Opt. **21,** 3569–3580 (1982).
9. Y. Takano and K. Jayaweera, "Scattering phase matrix for hexagonal ice crystals computed for ray optics," Appl. Opt. **24,** 3254–3263 (1985).
10. Y. Takano and K. N. Liou, "Solar radiation transfer in cirrus clouds. Part I: Single-scattering and optical properties of hexagonal ice crystals," J. Atmos. Sci. **46,** 3–19 (1989).
11. E. Tränkle and R. G. Greenler, "Multiple-scattering effects in halo phenomena," J. Opt. Soc. Am. A **4,** 591–599 (1987).
12. K. Muinonen, "Scattering of light by crystals: a modified Kirchhoff approximation," Appl. Opt. **28,** 3044–3050 (1989).

13. Y. Takano and K. N. Liou, "Radiative transfer in cirrus clouds. Part III: Light scattering by irregular ice crystals," J. Atmos. Sci. (to be published).
14. A. Macke, "Scattering of light by irregular ice crystals in the three-dimensional inhomogeneous cirrus clouds," presented at the Eighth Conference on Atmospheric Radiation, Nashville, Tenn., January 1994.
15. Y. Takano, K. N. Liou, and P. Minnis, "The effects of small ice crystals on cirrus infrared radiation properties," J. Atmos. Sci. **49,** 1487–1493 (1992).
16. E. M. Purcell and C. P. Pennypacker, "Scattering and absorption of light by nonspherical dielectric grains," Astrophys. J. **196,** 705–714 (1973).
17. B. T. Draine, "The discrete-dipole approximation and its application to interstellar graphite grains," Astrophys. J. **333,** 848–872 (1988).
18. P. Barber and C. Yeh, "Scattering of electromagnetic waves by arbitrarily shaped dielectric bodies," Appl. Opt. **14,** 2864–2872 (1975).
19. G. H. Goedecke and S. G. O'Brien, "Scattering by irregular inhomogeneous particles via the digitized Green's function algorithm," Appl. Opt. **27,** 2431–2438 (1981).
20. H. Y. Chen and M. F. Iskander, "Light scattering and absorption by fractal agglomerate and coagulations of smoke aerosols," J. Mod. Opt. **37,** 171–181 (1990).
21. S. K. Yee, "Numerical solution of initial boundary value problems involving Maxwell's equation in isotropic media," IEEE Trans. Antennas Propag. **AP-14,** 302–307 (1966).
22. A. Taflove and M. E. Brodwin, "Numerical solution of steady-state electromagnetic scattering problems using the time-dependent Maxwell's equations," IEEE Trans. Microwave Theory Tech. **MTT-23,** 623–630 (1975).
23. K. Umashankar and A. Taflove, "A novel method to analyze electromagnetic scattering of complex objects," IEEE Trans. Electromagn. Compat. **EMC-24,** 397–405 (1982).
24. C. L. Britt, "Solution of electromagnetic scattering problems using time domain techniques," IEEE Trans. Antennas Propag. **37,** 1181–1191 (1989).
25. A. Taflove, "Application of the finite-difference time-domain method to sinusoidal steady-state electromagnetic-penetration problems," IEEE Trans. Electromagn. Compat. **EMC-22,** 191–202 (1980).
26. M. Furse, S. P. Mathur, and O. P. Gandhi, "Improvements on the finite-difference time-domain method for calculating the radar cross section of a perfectly conducting target," IEEE Trans. Microwave Theory Tech. **38,** 919–927 (1990).
27. R. Holland, V. R. Cable, and L. C. Wilson, "Finite-volume time-domain (FVTD) techniques for EM scattering," IEEE Trans. Electromagn. Compat. **33,** 281–293 (1991).
28. Z. Liao, H. L. Wong, B. Yang, and Y. Yuan, "A transmitting boundary for transient wave analyses," Sci. Sin. **27,** 1063–1076 (1984).
29. B. Engquist and A. Majda, "Absorbing boundary conditions for the numerical simulation of waves," Math. Comput. **31,** 629–651 (1977).
30. G. Mur, "Absorbing boundary condition for the finite-difference approximation of the time-domain electromagnetic-field equations," IEEE Trans. Electromagn. Compat. **EMC-23,** 377–382 (1982).
31. J. G. Blaschak and G. A. Kriegsmann, "A comparative study of absorbing boundary conditions," J. Comput. Phys. **77,** 109–139 (1988).
32. T. G. Moore, J. G. Blaschak, A. Taflove, and G. A. Kriegsmann, "Theory and application of radiation boundary operators," IEEE Trans. Antennas Propag. **36,** 1797–1812 (1988).
33. M. Fusco, "FDTD algorithm in curvilinear coordinates," IEEE Trans. Antennas Propag. **38,** 76–89 (1990).
34. T. G. Jurgens, A. Taflove, K. Umashankar, and T. G. Moore, "Finite-difference time-domain modeling of curved surfaces," IEEE Trans. Antennas Propag. **40,** 357–366 (1992).
35. K. S. Yee, J. S. Chen, and A. H. Chang, "Conformal finite difference time domain (FDTD) with overlapping grids," IEEE Trans. Antennas Propag. **40,** 1068–1075 (1992).
36. M. A. Fusco, M. V. Smith, and L. W. Gordon, "A three-dimensional FDTD algorithm in curvilinear coordinates," IEEE Trans. Antennas Propag. **39,** 1463–1471 (1991).
37. J. F. Lee, "Obliquely Cartesian finite difference time domain algorithm," Proc. Inst. Electr. Eng. Part H, **140,** 23–27 (1993).
38. S. Omick and S. P. Castillo, "A new finite-difference time-domain algorithm for the accurate modeling of wide-band electromagnetic phenomena," IEEE Trans. Electromagn. Compat. **35,** 315–222 (1993).
39. H. Vinh, H. Duger, and C. P. Van Dam, "Finite-difference methods for computational electromagnetics (CEM)," in *IEEE AP-S International Symposium Digest*, (Institute of Electrical and Electronics Engineers, New York, 1992) Vol. 3, pp. 1682–1683 .
40. D. Steich, R. Luebbers, and K. Kunz, "Absorbing boundary condition convergence comparisons," in *IEEE AP-S International Symposium Digest* (Institute of Electrical and Electronics Engineers, New York, 1993), Vol. 1, pp. 6–9.
41. K. K. Mei and J. Fang, "Superabsorption—a method to improve absorbing boundary conditions," IEEE Trans. Antennas Propag. **40,** 1001–1010 (1992).
42. R. H. T. Bates, "Analytic constraints on electromagnetic computations," IEEE Trans. Microwave Theory Tech. **MTT-23,** 605–622 (1975).
43. C. F. Bohren and D. R. Huffman, *Absorption and Scattering of Light by Small Particles* (Wiley, New York, 1983), Chaps. 3 and 8.
44. M. Born and E. Wolf, *Principles of Optics* (Pergamon, New York, 1959), pp. 110–113, 377–399, 627–633, and 707–716.
45. J. A. Stratton and L. J. Chu, "Diffraction theory of electromagnetic waves," Phys. Rev. **56,** 99–107 (1939).
46. J. D. Jackson, *Classical Electrodynamics* (Wiley, New York, 1962), pp. 299–304.
47. E. A. Hovenac and J. A. Lock, "Assessing the contribution of surface waves and complex rays to far-field Mie scattering by use of the Debye series," J. Opt. Soc. Am. A **9,** 781–795 (1992).